

# An improved refractive index sensor based on genetic optimization of plasmon waveguide resonance

Farshid Bahrami,<sup>1,\*</sup> Mathieu Maisonneuve,<sup>2</sup> Michel Meunier,<sup>2</sup> J. Stewart Aitchison,<sup>1</sup> and Mo Mojahedi<sup>1</sup>

<sup>1</sup>Department of Electrical and Computer Engineering, University of Toronto, Ontario, M5S 3G4, Canada

<sup>2</sup>Department of Physics engineering, Ecole Polytechnique de Montreal, Montreal, H3C 3A7, Canada

\*farshid.bahrami@mail.utoronto.ca

**Abstract:** Plasmon waveguide resonance (PWR) sensors are particularly useful for biosensing due to their unique ability to perform sensing with two different polarizations. In this paper we report a comprehensive performance comparison between the surface plasmon resonance (SPR) sensor and the PWR sensor in terms of the sensitivity and the refractive index resolution. Both sensors were optimized using a genetic algorithm to acquire their best performance for bulk sensing applications. The experimental results show that the PWR sensor has a refractive index resolution of  $5 \times 10^{-7}$  RIU which is 6 times smaller than that of the optimized SPR sensor. The TE polarization in the PWR sensor has a resolution of  $1.4 \times 10^{-6}$  RIU which is smaller than the SPR sensor. The polarization diversity in the PWR sensor is another advantage which can be used to improve the measurement reliability.

©2013 Optical Society of America

**OCIS codes:** (280.4788) Optical sensing and sensors; (250.5403) Plasmonics; (230.7400) Waveguides, slab.

---

## References and links

1. X. Fan, I. M. White, S. I. Shopova, H. Zhu, J. D. Suter, and Y. Sun, "Sensitive optical biosensors for unlabeled targets: A review," *Anal. Chim. Acta* **620**(1-2), 8–26 (2008).
2. S. Janz, A. Densmore, D. X. Xu, P. Waldron, J. Lapointe, J. H. Schmid, T. Mischki, G. Lopinski, A. Del ge, R. McKinnon, P. Cheben, and B. Lamontagne, "Silicon photonic wire waveguide sensors," in *Advanced Photonic Structures for Biological and Chemical Detection*, X. Fan, ed. (Springer, 2009), pp. 229–264.
3. A. Shalabney and I. Abdulhalim, "Sensitivity-enhancement methods for surface plasmon sensors," *Laser and Photonics Reviews* **5**(4), 571–606 (2011).
4. A. Otto and W. Sohler, "Modification of the total reflection modes in a dielectric film by one metal boundary," *Opt. Commun.* **3**(4), 254–258 (1971).
5. Z. Salamon, M. F. Brown, and G. Tollin, "Plasmon resonance spectroscopy: Probing molecular interactions within membranes," *Trends Biochem. Sci.* **24**(6), 213–219 (1999).
6. Z. Salamon, H. A. Macleod, and G. Tollin, "Coupled plasmon-waveguide resonators: A new spectroscopic tool for probing proteolipid film structure and properties," *Biophys. J.* **73**(5), 2791–2797 (1997).
7. M. Zourob, S. Mohr, B. J. T. Brown, P. R. Fielden, M. McDonnell, and N. J. Goddard, "The development of a metal clad leaky waveguide sensor for the detection of particles," *Sens. Actuators B Chem.* **90**(1-3), 296–307 (2003).
8. N. Skivesen, R. Horvath, S. Thinggaard, N. B. Larsen, and H. C. Pedersen, "Deep-probe metal-clad waveguide biosensors," *Biosens. Bioelectron.* **22**(7), 1282–1288 (2007).
9. M. Zourob, S. Mohr, B. J. Brown, P. R. Fielden, M. B. McDonnell, and N. J. Goddard, "An integrated optical leaky waveguide sensor with electrically induced concentration system for the detection of bacteria," *Lab Chip* **5**(12), 1360–1365 (2005).
10. M. Zourob, S. Mohr, B. J. T. Brown, P. R. Fielden, M. McDonnell, and N. J. Goddard, "The development of a metal clad leaky waveguide sensor for the detection of particles," *Sens. Actuators B Chem.* **90**(1-3), 296–307 (2003).
11. J. S. A. F. Bahrami and M. Mojahedi, "A highly optimized plasmon waveguide resonance biosensor," in *IEEE Photonics Conference* (IEEE, 2012).
12. N. Skivesen, R. Horvath, and H. C. Pedersen, "Optimization of metal-clad waveguide sensors," *Sens. Actuators B Chem.* **106**(2), 668–676 (2005).

13. T. Lebyedyeva, Y. Frolov, S. Kurlov, M. Budnyk, Y. Minov, P. Sutkovyi, and P. Shpylovyi, "Modeling and data processing for thin-film optical sensors," in 6th IEEE International Conference on Intelligent Data Acquisition and Advanced Computing Systems: Technology and Applications, IDAACS (2011), 119–124.
14. H. Zhang, K. S. Orosz, H. Takahashi, and S. S. Saavedra, "Broadband plasmon waveguide resonance spectroscopy for probing biological thin films," *Appl. Spectrosc.* **63**(9), 1062–1067 (2009).
15. M. Zourob and N. J. Goddard, "Metal clad leaky waveguides for chemical and biosensing applications," *Biosens. Bioelectron.* **20**(9), 1718–1727 (2005).
16. M. Piliarik and J. Homola, "Surface plasmon resonance (SPR) sensors: Approaching their limits?" *Opt. Express* **17**(19), 16505–16517 (2009).
17. F. Bahrami, M. Z. Alam, J. S. Aitchison, and M. Mojahedi, "Dual polarization measurements in the hybrid plasmonic biosensors," *Plasmonics* **8**(2), 465–473 (2012).
18. A. Abbas, M. J. Linman, and Q. Cheng, "Sensitivity comparison of surface plasmon resonance and plasmon-waveguide resonance biosensors," *Sens. Actuators B Chem.* **156**(1), 169–175 (2011).
19. S. G. Alasag, N. Cansever, and M. M. Aslan, "Sensitivity enhancement of coupled plasmon-waveguide resonance sensors with gold-silver-alumina layers," in *Proc. SPIE* **8424**, Nanophotonics IV, 84243A (2012).
20. J. Holland, *Adaptation in Natural and Artificial Systems: An Introductory Analysis with Applications to Biology, Control, and Artificial Intelligence* (A Bradford Book, 1992).
21. D. P. Edward, *Handbook of Optical Constants of Solids* (Academic Press, 1997).
22. <http://www.ssens.nl/>.
23. G. Dyankov, M. Zekriti, and M. Bousmina, "Dual-mode surface-plasmon sensor based on bimetallic film," *Appl. Opt.* **51**(13), 2451–2456 (2012).
24. J. J. Chyou, S. J. Chen, C. F. Shu, C. S. Chu, Z. H. Shih, and C. Y. Lin, "Fabrication and metrology of an electro-optic polymer light modulator based on waveguide-coupled surface plasmon resonance," *OPTICE* **44**, 034001–034007 (2005).
25. G. J. Kovacs and G. D. Scott, "Optical excitation of surface plasma waves in layered media," *Phys. Rev. B* **16**(4), 1297–1311 (1977).

## 1. Introduction

Optical sensors are widely used for biosensing in several platforms [1]. Surface plasmon resonance (SPR) and dielectric waveguide (WG) sensors are two well-established optical biosensors which address the need for label free biosensing. Both techniques are based on detecting the change in the analyte refractive index occurring within the penetration depth of the evanescent field, also called the *probing depth*. Depending on how the evanescent field interacts with the analyte, biosensors can be classified into two general categories: a) bulk, and b) surface (affinity) biosensors. In the case of bulk biosensors, the probing depth ideally should be extended away from the sensing surface to strongly interact with the bulk fluid (analyte). On the other hand, in the case of affinity sensors, the probing depth should be localized close to the sensing surface in order to strongly interacts with a thin layer (a few nanometers) of biomaterial called the adlayer located on top of the sensing surface [2]. The small probing depth of the SPR [3] and dielectric WG [2] biosensors (<200nm), makes them suitable for detecting the refractive index variations in the vicinity of the sensing surface.

Another promising structure which simultaneously benefits from the high sensitivity of the SPR sensors and also the small resonance width of the dielectric WG sensors is Plasmon waveguide resonance (PWR). The PWR was initially introduced for optical sensing by Otto *et al.* [4], and was implemented by Salamon *et al.* [5], to measure the optical properties (thickness, complex refractive index) of anisotropic membrane systems. Coupled Plasmon Waveguide Resonances (CPWR) [6], Metal Clad Leaky Waveguide (MCLW) [7], and Metal Clad Waveguide (MCWG) [8], are other names that have been used to refer to this structure. The PWR consists of a glass substrate, a thin metallic layer, and a dielectric layer on the top of the metal. The role of the metallic layer is to excite the dielectric waveguide modes (transverse magnetic (TM), and transverse electric (TE)) under certain conditions. The large probing depth of the TM polarized light in the PWR sensor makes it suitable for bulk sensing and detecting large biomaterials such as bacteria [9, 10], while the small probing depth of the TE polarized light is ideal for surface sensing [11, 12]. In general, PWR sensors have been categorized in two different types [8]: a) the dip type which has tens of nanometers of metal with a relatively low imaginary permittivity [13, 14], b) the peak type with a thinner metallic layer (a few nanometers) with relatively large imaginary permittivity [15].

In this study, the dip type PWR sensor is proposed as a promising tool which can exceed the performance of the SPR sensor based on Kretschmann configuration in terms of its

refractive index resolution [16]. Using a genetic algorithm, we have identified the conditions under which both PWR and SPR performances are optimum (in terms of their resolution). We have then fabricated and tested these sensors and have compared their performances for both TM and TE in the case of the PWR and only the TM mode in the case of SPR sensor. The ability of the PWR to operate in both TE and TM modes is an important characteristic of these sensors which allows the user to remove the influence of some interfering effects as discussed in [17]. Lastly, although some evaluation of the PWR in comparison to the SPR sensor has been carried out in Refs [12,14,18,19], to the best of our knowledge, there has been no comprehensive optimization and evaluation based on the refractive index resolution between these two configurations.

## 2. Modeling and optimization

Figure 1(a) shows the PWR sensor in the Kretschmann configuration, in which light is incident on the substrate through a prism and the reflected light intensity is measured as a function of the angle of incident. To model the PWR sensor, a transfer matrix method is used [9].

In order to conduct a fair comparison between the performances of the PWR and SPR sensors, a figure of merit (FoM) based on the refractive index resolution ( $\sigma_{RI}$ ) is defined. This FoM, called combined sensitivity factor (CSF), is the product of the sensor's sensitivity also called sensitivity factor (SF) and its spectrum linewidth also called sensor merit (SM) in this work. In [18], it was shown that the aforementioned CSF is inversely proportional to the refractive index resolution and can be written as:

$$CSF_{bulk} = SF \times SM = \frac{\partial \theta_{res}}{\partial n_b} \times \frac{R_{max} - R_{min}}{FWHM} \propto \frac{1}{\sigma_{RI}}. \quad (1)$$

Here,  $\theta_{res}$  is the resonance angle,  $n_b$  is the bulk refractive index,  $FWHM$  is the full width at half maximum, and  $R_{max}$  and  $R_{min}$  are the maximum and minimum reflectance, respectively [17]. For brevity, hereon, we refer to the bulk CSF simply as the CSF.

We have used a genetic algorithm as is described in [17]– with the above CSF as its “fitness function” [20], – to determine the wavelength of operation and layer thicknesses (in the case of the PWR) which maximizes the CSF (i.e., minimizes the resolution) for both sensors. In Table 1, the optimized design parameters for both structures for bulk sensing application are listed.

In our calculations there are a few points worth mentioning: 1) We have assumed that the substrate and prism are both BK7 glass. 2) Gold is used as the metallic layer in both sensors, which is a preferred plasmonic layer. 3) For our calculations we have used the material optical properties listed in Palik [21]. 4) Both sensors have 2nm titanium layer between the substrate and the gold layer in order to improve the gold adhesion to the substrate.

**Table 1. Comparison of the optimized PWR and SPR sensors' characteristics**

Sensor	Layers	Optimized parameters	polarization	SF (deg./RIU)	SM (deg. <sup>-1</sup> )	CSF (RIU <sup>-1</sup> )
PWR	1. BK7 glass 2. Titanium 3. Gold (d) 4. Silica(h)	h=925nm d=44nm λ=1200nm	TM	78	42	3276
			TE	21	14	294
SPR	1. BK7 glass 2. Titanium 3. Gold (d)	d=46nm λ=1230nm	TM	90	2	180

Figure 1(b) shows the calculated reflectance spectrum for both optimized sensors. The resonance curves of both TM and TE polarizations (black and red lines in Fig. 1(b)) in the PWR sensor are much sharper than the SPR resonance curve (blue line). Figures 1(c) and 1(d) show the spatial distribution of the power density (poynting vector) along the propagation

direction ( $z$ ) as a function of the vertical direction ( $x$ ), for the optimized PWR and the SPR sensors at their corresponding resonance angles, respectively. In the PWR sensor, the TE mode is mostly confined in the top silica layer (red line in Fig. 1(c)) where its penetration depth into the bulk fluid is 270nm. On the other hand, the TM polarization intensity is mostly localized inside the cover layer (fluid) with its highest intensity at the silica-fluid interface. The penetration depth of the PWR-TM mode inside the fluid is 9 $\mu$ m which makes it suitable for bulk sensing. Finally, the calculated penetration depth of the optimized SPR-TM mode (the only mode supported by this sensor) is 460nm, as shown in Fig. 1(d).

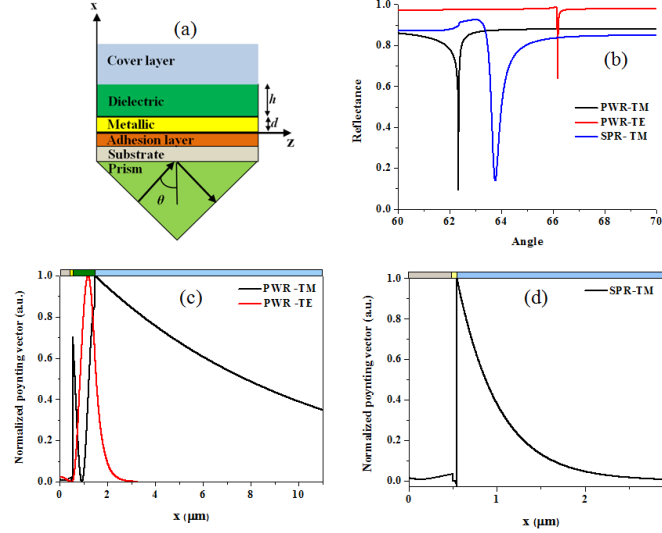


Fig. 1. (a) Schematic diagram of the PWR sensor. (b) Reflectance spectrum for the optimized PWR-TM, PWR-TE, and SPR-TM polarizations in black, red, and blue lines, respectively. (c)  $z$ -component of the Poynting vector for both TM and TE polarizations in the optimized PWR sensor at the resonance angle of 62.35° and 66.18°, respectively. (d)  $z$ -component of the Poynting vector for the TM polarization in the optimized SPR sensor at the resonance angle of 63.77°.

Before presenting our experimental results in the next section, it is useful to discuss tolerance of the PWR and SPR sensors with respect to fabrication imperfections. Figure 2(a) shows the variations of the CSF for the SPR sensor with respect to the incident wavelength. As evident from the Fig. 2(a), the CSF is maximum at ~1200nm. The tolerance of the PWR sensor with respect to silica thickness at different wavelengths for the TM and TE polarizations are shown in Figs. 2(b) and 2(c), respectively. As evident from the Figs., the PWR-TE mode is less sensitive to fabrication imperfections than the PWR-TM mode. However, it is possible to maximize the CSF for the PWR-TM polarization by tuning the incident wavelength for any silica thickness.

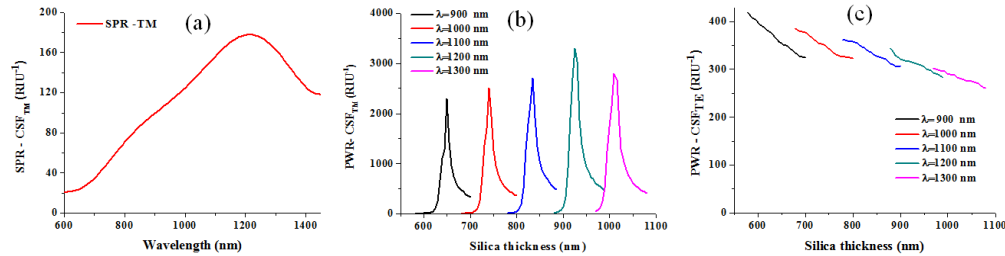


Fig. 2. (a) The CSF variation along with the incident light wavelength in the optimized SPR sensor. The CSF variation along with the silica thickness at different wavelengths in the PWR sensor for (b) TM and (c) TE polarizations.

### 3. Materials and methods

#### 3.1 Sensors fabrication

We obtained BK7 glass substrates, with a size of  $1\text{cm} \times 1\text{cm}$ , coated with  $48 \pm 1\text{nm}$  gold layers from the SSENS Ltd [22]. In order to ensure good adhesion of the gold film to the glass substrate, a thin layer of titanium (2 nm) was introduced between the glass and the gold film. These samples, which were used as our SPR reference sensors, were initially cleaned with a piranha solution at  $90^\circ\text{C}$  for 20min to remove organic contaminations. After the initial cleaning, the samples were further cleaned in an ultrasonic bath with acetone, isopropanol, and deionized water for 10 minutes each.

The same gold plated samples from SSEN were used to fabricate our PWR sensors. For this propose a silica layer of specific thickness (see below) was deposited on the gold film using a plasma enhanced chemical vapor deposition (PECVD) by mixing silane ( $\text{SiH}_4$ ) and nitrous oxide ( $\text{N}_2\text{O}$ ) in vacuum at approximately  $300^\circ\text{C}$ .

#### 3.1 Instrumentation

Figure 3 shows the optical setup used to characterize the performances of the PWR and SPR sensors. In this setup, an optical beam from a super continuum laser (Fianium SC-450) is passed through a laser line tunable filter (Photon Etc) in order to provide excitation at different wavelengths with a bandwidth less than 2nm. A single mode optical fiber is attached to the output of the filter which directs the light to an achromatic lens (L1) in order to collimate the light rays. The collimated light is then passed through a polarizer (P) and another achromatic lens (L2) in order to achieve a converging beam to cover a desired range of angles. The converging beam is focused onto the SPR or PWR sensor(s) which is (are) attached with immersion oil (Cargile Lab) to a prism back surface. This sensing block (prism and the sample) is fixed to a flow cell in which a desired mixture of fluids flows. Finally, the diverging light that is reflected from the sample (sensor) surface is collected by a CMOS camera (Thorlabs) to analyze the angular spectrum of the beam intensity. A Labview program was written to process the image recorded by the CMOS camera which in addition determines the minimum position of the angular curves by using a polynomial interpolation.

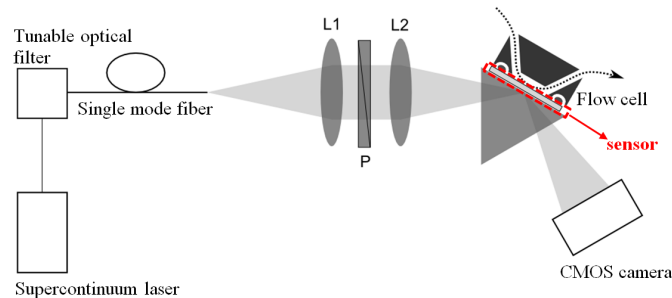


Fig. 3. Proposed optical setup for minimum position measurement.

### 4. Results and discussions

Two different kinds of measurements are used to study the effects of bulk index variations on the sensors' performances. The first kind is a static measurement which involves the analysis of the entire resonance curve with respect to the line shape changes as a function of time. This analysis provides a better insight from the sample under study since more information can be extracted from the resonance shape: the resonance width (FWHM), the resonance depth, and the resonance angle. The second kind is a dynamic measurement which is based on the analysis of the biological alteration only by tracing the variations in the resonance angle. This measurement is useful for real time analysis of the sample under studied.

We should point out that the values for silica and gold thicknesses ( $h$  and  $d$ ) given in Table 1 will result in the largest CSF (the smallest resolution) for the PWR and SPR sensors. The wavelengths of operation corresponding to these large values of CSFs are 1200nm and 1230nm for the PWR and SPR, respectively. However, the CMOS camera available in our setup (Fig. 3) has better sensitivity to wavelengths less than or equal to 900nm. Therefore, we had to rerun our optimization algorithm with the constraint that the wavelength of operation remains less than or equal to 900nm for both sensors. The results of this analysis are presented in Table 2. By comparing the data in Tables 2 and 3 it is seen that the performance of the PWR in the TM mode suffers the most as the result of enforcing the practical limitations of our experimental setup. The PWR sensor fabricated has silica thickness of 585nm which was measured using an ellipsometer.

**Table 2. Comparison of the optimized PWR and SPR sensors' characteristics with considering the limitations in the given setup**

Sensor	Optimized parameters	polarization	SF (deg./RIU)	SM (deg. <sup>-1</sup> )	CSF (RIU <sup>-1</sup> )
PWR	$h = 585\text{nm}$	TM	78	22	1716
	$d = 48\text{nm}$				
	$\lambda = 830\text{nm}$	TE	13	22	286
SPR	$d = 48\text{nm}$ $\lambda = 900\text{nm}$	TM	97	1	97

#### 4.1 Static measurements

In this experiment, the reflectance intensity is monitored versus the angle of incident. To prove the concepts predicted by the simulation, two different wavelengths are used for comparison: 1) He-Ne wavelength ( $\lambda = 632\text{nm}$ ) which is a common wavelength used in biosensing experiments [5, 23, 24] and 2) a wavelength close to the optimized wavelength for each sensor. Figures 4(a) through 4(c) show the reflectance spectrum of both sensors with respect to the incident light angle at the He-Ne wavelength. These spectrums are recorded for different concentrations of ethanol solutions over the sample. As explained earlier, the SPR resonance curve (Fig. 4(c)) is much wider than the PWR curves (Figs. 4(a) and 4(b)). The simulated results for both PWR and SPR sensors are shown in Figs. 4(d) through 4(e) which are in good agreement with the experimental results. The effects of surface roughness is compensated in the simulation by using Maxwell Garnett theory [25]. However, the small difference between the experimental and theoretical results can be due to several reasons like fabrication imperfections, the presence of matching oil index and also the light source bandwidth.

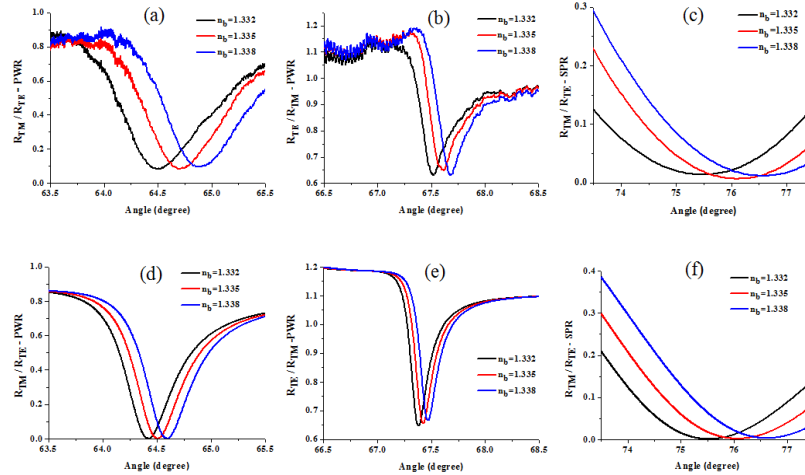


Fig. 4. The experimental normalized reflectance spectrum at  $\lambda = 632\text{nm}$  for (a) TM-polarized PWR sensor. (b) TE polarized PWR sensor. (c) TM-polarized SPR sensor. The theoretical normalized reflectance spectrum at  $\lambda = 632\text{nm}$  for (d) TM-polarized PWR sensor. (e) TE polarized PWR sensor. (f) TM-polarized SPR sensor. The different curves refer to reflectance spectrum for different concentrations of ethanol solution, 0.7% (red), 7% (blue). The water spectrum (black) is the reference.

In Table 3, the measured sensors characteristics at the He-Ne wavelength are compared with the theoretical results. As can be seen from this table, the SPR sensor has much larger sensitivity than the PWR at this wavelength but its smaller SM results in small CSF.

**Table 3. Experimental and theoretical sensors' characteristics for the fabricated PWR and SPR sensors at  $\lambda = 632\text{ nm}$**

Sensor	polarizations	SF (deg./RIU)		SM (deg. <sup>-1</sup> )		CSF (RIU <sup>-1</sup> )	
		Experiment	Theory	Experiment	Theory	Experiment	Theory
PWR	TM	43	36	0.88	1.07	38	37
	TE	16	15	1.1	2	17	30
SPR	TM	206	178	0.06	0.08	12	14

Figure 5(a) shows the normalized reflectance spectrum for both polarizations in the PWR sensor at the optimized wavelength (830nm). The resonance curve is sharper than that at He-Ne wavelength (Figs. 4(a) and 4(b)). The same trend is observed from the SPR sensor at  $\lambda = 900\text{nm}$  (Fig. 4(b)) compared with He-Ne wavelength.

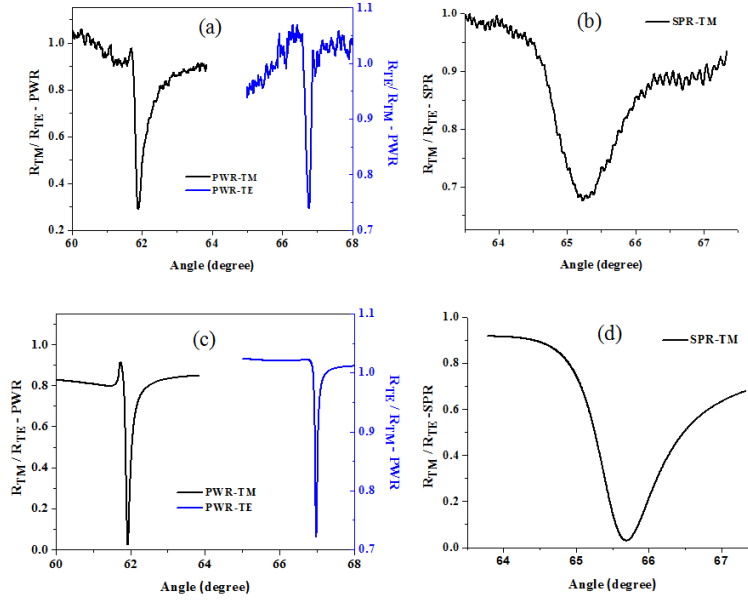


Fig. 5. The experimental normalized reflectance spectrum for (a) TM-polarized (black) and TE-polarized (blue) PWR sensor at  $\lambda = 830\text{nm}$  (b) TM-polarized SPR sensor at  $\lambda = 900\text{nm}$ . The theoretical normalized reflectance spectrum for (c) TM-polarized (black) and TE-polarized (blue) PWR sensor at  $\lambda = 830\text{nm}$  (d) TM-polarized SPR sensor at  $\lambda = 900\text{nm}$ .

The measured sensors characteristics corresponding to the results shown in Fig. 5 are presented in Table 4. The measured CSF for the PWR-TM polarization is  $322 \text{ RIU}^{-1}$  at  $\lambda = 830\text{nm}$  which is almost an order of magnitude larger than the CSF in SPR sensor at  $\lambda = 900\text{nm}$  ( $48 \text{ RIU}^{-1}$ ). Therefore, by optimizing the wavelength, the CSF has been improved in both sensors as compared to the results at the He-Ne wavelength. However, the improvement in the PWR sensor performance ( $\text{CSF}_{\text{TM}}$  and  $\text{CSF}_{\text{TE}}$ ) is much larger than that of the SPR sensor ( $\text{CSF}_{\text{TM}}$ ).

**Table 4. Experimental and theoretical sensors' characteristics for the fabricated SPR Sensor at  $\lambda = 900 \text{ nm}$  and the PWR sensor at  $\lambda = 830 \text{ nm}$**

Sensor	polarizations	SF ( $\text{deg./RIU}$ )		SM ( $\text{deg.}^{-1}$ )		CSF ( $\text{RIU}^{-1}$ )	
		Experiment	Theory	Experiment	Theory	Experiment	Theory
PWR	TM	164	113	1.95	3.7	320	322
	TE	36	23	1.82	4	66	92
SPR	TM	125	97	0.27	0.49	35	48

#### 4.2 Dynamic measurements

In the case of dynamic measurements, at a given wavelength, the resonance angle variation is monitored (in real time) while the concentration of the solution is changed. We prepared three different solutions with 0.5%, 1%, and 2% of ethanol in deionized water to create bulk refractive index changes of 0.00014, 0.00028, and 0.00056 RIU, respectively. Pure deionized water is first passed over the sample for 5min to create a baseline. Then an ethanol solution with low concentration (0.5%) is passed for another 5min. After that, again, deionized water flows over the sample to recreate the baseline and the same steps are repeated for higher concentrations.

Figure 6(a) shows the PWR sensor response at  $\lambda = 632\text{nm}$  and  $\lambda = 830\text{nm}$  for TM polarization. The small slope of the baseline is due to the heat generated caused by wave propagation at metal dielectric interface. Figure 6(d) shows the same response with adjusted baseline to coincide with zero. Figure 6(b) show the PWR response for TE polarization and the baseline is adjusted in Fig. 6(e). The larger sensitivity of the PWR-TM polarization, as



compared to the PWR-TE polarization, can be seen by comparing the change in the resonance angles in Figs. 6(d) and 6(e). Also the TE polarization has smaller thermal drift in the baseline since the mode is more confined inside the top dielectric layer [Fig. 1(c)] while the TM polarization has larger intensity at metal dielectric interface [Fig. 1(c)] which causes more heat generation due to large thermal conductivity of the gold layer. Fig. 6(c) shows the SPR response (only TM polarization) to variations of the bulk index at  $\lambda = 632\text{nm}$  and  $\lambda = 900\text{nm}$  and the baseline is adjusted in Fig. 6(f). The larger thermal drift of the baseline in SPR sensor can be observed by comparing the baselines of both PWR and SPR sensors. This large thermal drift is due to the fact that the metal layer is in direct contact with the fluid in SPR sensor while in PWR sensor there is a thick dielectric spacer between the metal and the fluid. According to Fig. 6(f), the sensitivity of the SPR sensor is larger at  $\lambda = 632\text{nm}$ .

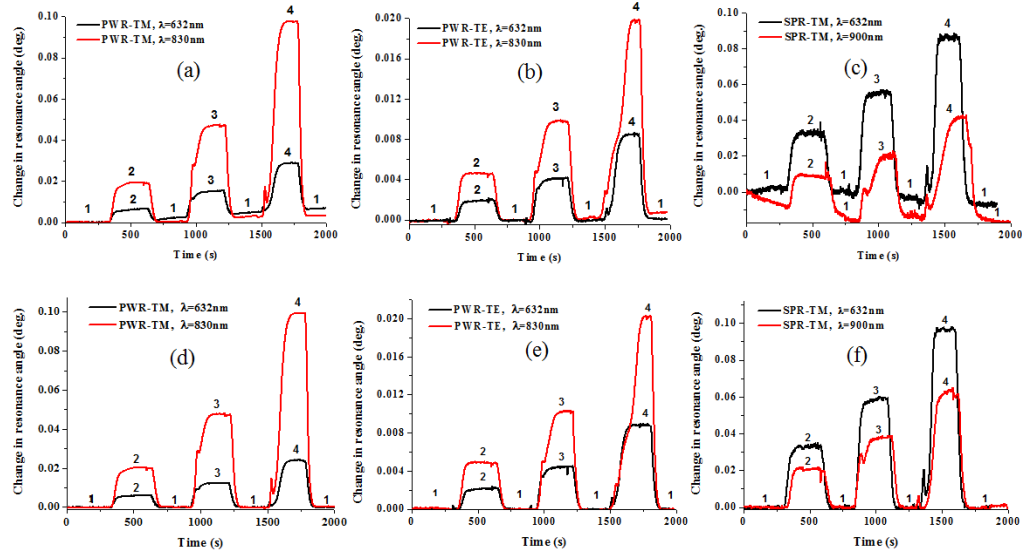


Fig. 6. Sensors' responses to the bulk refractive index variations: (a) Resonance angle versus time for the TM-polarized PWR sensor at  $\lambda = 632\text{nm}$ , and  $830\text{nm}$  (b) Resonance angle versus time for the TE-polarized PWR sensor at  $\lambda = 632\text{nm}$ , and  $830\text{nm}$  (c) Resonance angle versus time for the TM-polarized SPR sensor at  $\lambda = 632\text{nm}$ , and  $900\text{nm}$ . Sensors' responses to the bulk refractive index variations with baseline adjusted to zero: (d) Resonance angle versus time for the TM-polarized PWR sensor at  $\lambda = 632\text{nm}$ , and  $830\text{nm}$  (e) Resonance angle versus time for the TE-polarized PWR sensor at  $\lambda = 632\text{nm}$ , and  $830\text{nm}$  (f) Resonance angle versus time for the TM-polarized SPR sensor at  $\lambda = 632\text{nm}$ , and  $900\text{nm}$ . Solutions are based on (1) DI water, (2) 0.5% ethanol, (3) 1% ethanol (4) 2% ethanol.

Table 5 presents the measured sensors' characteristics for both sensors at different wavelengths. The refractive index resolution of a sensor ( $\sigma_{RI}$ ) is related to the standard deviation of the sensor output ( $\sigma_{SO}$ ), sensitivity, and signal-to-noise ratio (SNR) according to [16]:

$$\sigma_{RI} \equiv \frac{\sigma_{SO}}{SF} = \frac{1}{SNR}. \quad (2)$$

As evident from Table 5 both PWR polarizations (TM and TE) have smaller standard deviation than the SPR-TM polarization. This is due to the PWR sharper resonance which produces larger SM. The standard deviation of the SPR sensor reduces with increasing wavelength due to its larger SM at longer wavelengths, so the refractive index resolution of the SPR at  $900\text{nm}$  is a smaller number as compared to the resolution at  $632\text{nm}$ .

**Table 5. Experimental sensors' characteristics calculated from the sensograms shown in Fig. 6**

Sensor	Polarization	Wavelength (nm)	$\overline{SF}$ (deg./RIU)	$\overline{\sigma_{SO}}$ (deg.)	$\overline{\sigma_{RI}}$ (RIU)
PWR	TM	632	43	$9.7 \times 10^{-5}$	$2.3 \times 10^{-6}$
		830	164	$8.2 \times 10^{-5}$	$5 \times 10^{-7}$
	TE	632	16	$4.6 \times 10^{-5}$	$2.9 \times 10^{-6}$
		830	36	$5.1 \times 10^{-5}$	$1.4 \times 10^{-6}$
SPR	TM	632	206	$6.6 \times 10^{-4}$	$3.2 \times 10^{-6}$
		900	125	$3.8 \times 10^{-4}$	$3 \times 10^{-6}$

There are a few important points worth mentioning: 1) The measured values of the standard deviations ( $\overline{\sigma_{SO}}$ ,  $\overline{\sigma_{RI}}$ ) and  $\overline{SF}$  which are included in Table 5 are the average values. 2) Standard deviations of the PWR waveguide modes are smaller than the standard deviation of the SPR sensor which makes the average resolution for both PWR modes smaller than the SPR. This is due to the fact that, the SMs of the PWR waveguide modes are larger than the SM of the SPR (see Table 3 and Table 4). A narrow resonance curve (i.e., a large SM) along with a large SF (Eq. (1)) results in performance improvement for the PWR in detecting the smallest change in the refractive index [17]. 3) The change in the resolution for the SPR sensor with respect to the excitation wavelength is much smaller than that in each polarizations of the PWR sensor. 4) The PWR modes [Figs. 6(a) and 6(b)] are less sensitive to temperature fluctuations than the SPR [Fig. 6(c)] which results in a much smaller adjustment for the PWR sensors. This is due to the fact that in the SPR sensor, the gold layer, which has large thermal conductivity, is in direct contact with the fluid while in the PWR sensor there is a thick dielectric layer between the gold and the fluid on top which has small thermal conductivity. Therefore, the heat generated by the gold has less influence on the fluid refractive index in the PWR sensor. 5) The polarization diversity in the PWR sensor can be used to remove the interfering surface and bulk effects, to eliminate the need for an ideal reference channel (self-reference measurements) [18], and to increase the measurement reliability by performing multiple independent measurements on the same sample.

## 5. Conclusion

A PWR sensor was proposed as a promising tool for bulk sensing applications. It was demonstrated that its sharp resonance curves and high sensitivity can result in a smaller refractive index resolution than the conventional SPR sensor. The performance of the PWR and SPR sensors has been optimized using a genetic algorithm. The optimized structures have been tested with an angular modulation setup. The measured refractive index resolution in the PWR sensor is  $5 \times 10^{-7}$  RIU and  $1.4 \times 10^{-6}$  RIU for TM and TE polarizations, respectively; and the refractive index resolution for the SPR sensor is  $3 \times 10^{-6}$  RIU for the TM polarization. The improvement in the resolution for the PWR sensor is attributed to the smaller standard deviation of the detector noise level which itself can be traced back to its sharper resonance curves. The polarization diversity of the PWR can be used to improve the measurement reliability.

## Acknowledgments

We would like to acknowledge the use of computing resources from West Grid. This work was supported by the Natural Science and Engineering Research Council of Canada–Biopsys Network under grant no. 486537.